



Study on Combustion Characteristics and Flame Flow Behavior with Ethanol-Kerosene Mixed Fuel in HVOF Spraying

Siyu Li¹ · Chang Li¹ · Pengfei Liu¹ · Xing Han¹

Submitted: 19 April 2024 / in revised form: 28 June 2024 / Accepted: 10 July 2024
© ASM International 2024

Abstract Aviation kerosene is a high-density, high-calorific value fuel widely used in high-velocity oxygen fuel (HVOF) thermal spraying. However, incomplete combustion of aviation kerosene generates CO₂, CO, and unburned hydrocarbons, which are not conducive to sustainable development for industry. Research on new HVOF processes using clean fuels is significant for energy conservation and emission reduction. In this study, a two-dimensional numerical model of JP-8000 spray gun flow field was established based on the computational fluid dynamics method, and the ethanol was blended into aviation kerosene fuel to reduce carbon emissions during spraying. Ethanol-kerosene premixed fuel and WC-12Co particles were injected into spray gun in discrete phase form. The KHRT method and O'Rourke method in the discrete phase model were used to deal with the breakup and coalescence of fuel droplets. Lagrange tracking method was used to capture the flight trajectory of fuel droplets and sprayed particles, and the gas-liquid-solid coupling calculation of spraying flow field was realized. The results show that adding ethanol to aviation kerosene fuel can effectively reduce CO₂ emissions. When the ethanol proportion is 10%, CO₂ emissions decrease by nearly 30%. Ethanol pyrolysis leads to a slight increase in CO emissions, which can be effectively reduced by appropriately increasing the oxygen/fuel ratio. This study provides an important theoretical basis for the spraying practice of HVOF mixed fuel for energy saving

and environmental protection and offers new insights for further optimizing the spraying process.

Keywords Ethanol-kerosene mixed fuel · HVOF thermal spraying · WC-12Co · Carbon emission

List of Symbols

A	Model constant 4
A_0	Model constant 4.04
A_s	Model constant $\sqrt{6}\cos\phi$
B	Model constant 0.5
C_μ	Dynamic viscosity coefficient
C	Constants, $C_I = \max[0.43, \eta/(\eta + 5)]$, $\eta = S_k/\varepsilon$, $C_2 = 1.9$, $C_{1\varepsilon} = 1.44$, $C_{2\varepsilon} = 0.09$
$c_{s,g}$	Heat transfer between droplets and gas
C_s	Droplet specific heat
d_p	Discrete phase diameter
d_s	Droplet diameter
E_M	Pulsation expansion on the total dissipation rate
E	Enthalpy value
G_k, G_b	Turbulent kinetic energy
h_{fg}	Latent heat
h	Convective heat transfer coefficient
$J_{\alpha,i}$	Mass diffusion flux
k	Kinetic energy
k_e	Heat conductivity coefficient
k_0	Partition coefficient
m_s	Droplet mass
m_p	Particle mass
M_i	Specie molecular weight
n	Size distribution index
N	Chemical components number
P	Gas pressure
Pr	Prandtl number of the continuous phase

Siyu Li and Chang Li are co-first authors of the article.

✉ Chang Li
lichang2323-23@163.com

¹ School of Mechanical Engineering and Automation, University of Science and Technology Liaoning, Anshan 114051, Liaoning, China

Re	Relative Reynolds number
R_α	Substance net productivity
S	Droplet surface area
S_α	Productivity
S_O	Source item
S_t	Chemical energy source term
S_k	Total kinetic energy term
S_ε	Turbulent dissipation rate source term
t	Turbulent time
T	Turbulent environment
T	Temperature
T_g	Gas temperature
T_s	Droplet temperature
T_p	Particle temperature
u	Flow velocity
u_i	Velocity in the i direction
u_j	Velocity in the j direction
u_p	Particle velocity
ν	Viscosity coefficient of molecular motion
$\nu''_{j,r}$	Stoichiometric coefficient of product j in reaction r
$\nu''_{i,r}$	Stoichiometric coefficient of reactant i in reaction r
$\vec{\nu}$	Phase transition mass flow rate
x	Coordinate values
Y_P	Mass fraction of the product P
Y_M	Effect of turbulence on total dissipation rate
Y_R	Mass fraction of the product R
Y_α	Mass fraction of the reactant
θ_s	Radiation temperature
ε	Turbulent dissipation rate
ε_s	Particle emissivity
μ_t	Turbulent viscosity
ρ	Density
$\vec{\Delta F}$	Additional force
$(\tau_{ij})_e$	Deviatoric stress tensor
ρ_s	Particle density
σ_ε	Prandtl number of turbulent dissipation rate
σ_k	Prandtl number of turbulent kinetic energy
σ	Stefan-Boltzmann constant

Introduction

Thermal spraying is a new surface strengthening technology. Compared to traditional chrome plating, coatings produced by HVOF have advantages such as low porosity, high bond strength, hardness, and deposition rates (Ref 1-4). It has been widely used in the production of piston ring and cylinder hole coatings in the automotive industry, roll and blade coatings in the paper industry, ball valve and gate valve coatings in the process industry, and thermal

barrier coatings for turbines and landing gear in the aerospace industry. With the rapid development of industry, the environmental burden is increasing, and the environmental protection requirements for the spraying process are increasing day by day. The thermal spraying process involves the combustion of flammable and explosive gases under high pressure, and dust pollution caused by micro- and nanospraying powder also occur during spraying, resulting in certain environmental damage (Ref 5). How to accurately control the process parameters and effectively reduce the pollution in spraying are significant for energy conservation and environmental protection.

The negative impact of thermal spraying technology on atmospheric environment is mainly attributed to the large amounts of pollutants produced by incomplete combustion of fuel during the spraying process. Commonly used fuels for spraying include hydrogen and hydrocarbons such as the ethylene, propylene, propane, natural gas, and aviation kerosene (atomized liquids) (Ref 4) in which aviation kerosene ($C_{12}H_{23}$) is one of the main fuels used in HVOF thermal spraying, and its combustion products contain a large amount of CO and CO_2 . That increases carbon emissions, aggravates the atmospheric "greenhouse effect," and leads to rising sea levels and ocean acidification, severely damages the ecosystem (Ref 6). Relevant research indicates that the combustion of aviation kerosene significantly impacts environment. As a clean and renewable fuel, the ethanol is considered as one of the ideal alternative fuels for aviation kerosene. To save fossil fuels, help "carbon peak, carbon neutrality," and promote industrial green development, this paper adopts ethanol-kerosene mixed fuel and reduces carbon emissions as much as possible under ensuring spraying performance.

The oxygen/fuel ratio (O/F) and fuel types in HVOF thermal spraying have important effects on coating performance (Ref 7). In the implementation of HVOF thermal spraying process, it is often in a fuel-rich combustion state, and the oxygen proportion in the spray gun is relatively less, to reduce the oxide proportion in the metal coating. When the spraying is in a fuel-rich combustion state, it is easy to cause insufficient combustion and produce a large amount of CO and other gases, causing pollution to the environment. Quantitatively revealing the combustion reaction state and effectively reducing the pollutant proportion in spraying are significant for improving the energy-saving and environmental protection effect of spraying process. The numerical simulation method can directly show the physical and chemical changes of fuel during spraying, and quantitatively reveal the reaction mechanism for ethanol-kerosene combustion, which helps determine the optimal value of fuel mixing ratio. Patra et al. (Ref 8) studied the effects of kerosene and ethanol-kerosene mixed fuel on flame characteristics in combustion

chamber, respectively. They captured flame images with high-velocity camera to reveal flame behaviors under different fuels. The results show that the mixed fuel burns more fully and only has less CO₂ proportion in the exhaust gas, which reduces the environmental carbon load. H. Tabbara (Ref 9) et al injected droplets in the form of discrete phase into the spray gun, and found that fuel droplets were broken and vaporized under the acceleration of flame during combustion. The droplet breakup method was studied in detail. Combined with the droplet thermo-physical properties, the primary and secondary breakup mechanisms were captured and compared with the time scales involved in droplet gasification. Wang et al. (Ref 10) simulated the flow field for HVOF thermal spraying by non-premixed combustion model, and explored the effects of turbulence intensity at oxygen and fuel inlet, oxygen/fuel ratio and fuel droplet size. The results show that when the droplet size is between 10 and 20 μm, the degree of fuel atomization significantly effects the flame flow characteristics (temperature, velocity and evaporation rate). Liu et al. (Ref 11) used ethanol as fuel to spray WC-10Co-4Cr powder by HVOF process, studied the effects of different oxygen/fuel ratios on particle flight velocity and temperature, further explored the performance of WC-CoCr coating, and elaborated the relationship between particle parameters and coating performance. They found that the ethanol fuel can easily lead to poorer particle temperature compared with other fuels. Jadidi et al. (Ref 12) adopted the two-way coupling Eulerian–Lagrangian method to establish a three-dimensional suspended HVOF spraying model including premixed combustion of oxygen-propylene and non-premixed combustion of oxygen-ethanol and oxygen-glycol. They combined with the Taylor Analogy model to simulate the droplet breaking; after the droplet breaking was complete, the solid particles were tracked to determine the characteristics of the particles.

In summary, the fuel type directly affects the combustion reaction, which in turn affects the flame flow and particle flight state in spraying. Although the use of ethanol fuel instead of aviation kerosene can save energy and reduce emission, the energy density of ethanol is poor, which decreases the binding strength of the coating and the substrate. At present, there is a lack of relevant research on the influence of ethanol-kerosene mixed fuel on the spraying process, and it is important to quantitatively reveal the influence for ethanol combustion on the spraying process. In this study, the kerosene and ethanol droplets were injected into the spray gun in discrete phases to explore the evolution process for fuel droplet breakup and gasification in the combustion chamber. The mixed combustion of ethanol-kerosene was optimized to achieve low pollution and high energy effects in spraying. This study has guiding significance for optimizing spraying fuel,

reducing industrial pollution and helping to achieve “carbon peak, carbon neutrality.”

The gun model used in this study is the JP-8000 spray gun produced by Praxair-Tafa (Ref 13–15). The fuel droplets are broken, gasified and burned in the combustion chamber, and the temperature of the reaction product rapidly rises under the impetus of heat, and the gas volume violently expands, and then forms a high-temperature, high-pressure flame. The spray powder is radially fed into a high-velocity flame by the inert gas, where it is heated, accelerated, and sprayed onto the surface of the pretreatment substrate to form a high-quality coating (Ref 16). HVOF spraying process and fuel droplet atomization model are shown in Fig. 1.

Numerical Modeling of the HVOF Spraying Process

Work Summary

The aim of this study is to introduce green fuel ethanol into the spraying process by numerical simulation, and provide a solid theoretical basis for the practice of the new ethanol-kerosene mixed fuel process. The evolution process of liquid fuel droplet breakup and gasification in combustion chamber was studied, and the influence of ethanol fuel on spraying process was quantitatively revealed. The process parameters of ethanol-kerosene mixed combustion spraying were further optimized to reduce carbon emission. The specific modeling steps are as follows:

1. According to the internal geometry size of JP-8000 spray gun and the size of the free stream, a parametric geometric model was established by using Ansys finite element analysis preprocessing software, and quadrilateral elements were used to divide the grid to establish the calculation area, and the geometric boundaries were named to facilitate the setting of boundary condition parameters.
2. A gas phase model was set for the calculation region, including continuity, momentum, energy and specie transport equations, and the realizable k - ϵ model was used to solve the turbulence problem. An eddy dissipation model (EDM) was used to simulate the combustion reaction during spraying.
3. Based on the gas phase model, discrete modeling of liquid fuel droplets and WC-12Co particles was carried out based on the Lagrange method, and gas–liquid–solid coupling was realized to determine the trajectory of particles and droplets.
4. The discrete equations were solved in a two-dimensional, axisymmetric, transient environment. The semi-

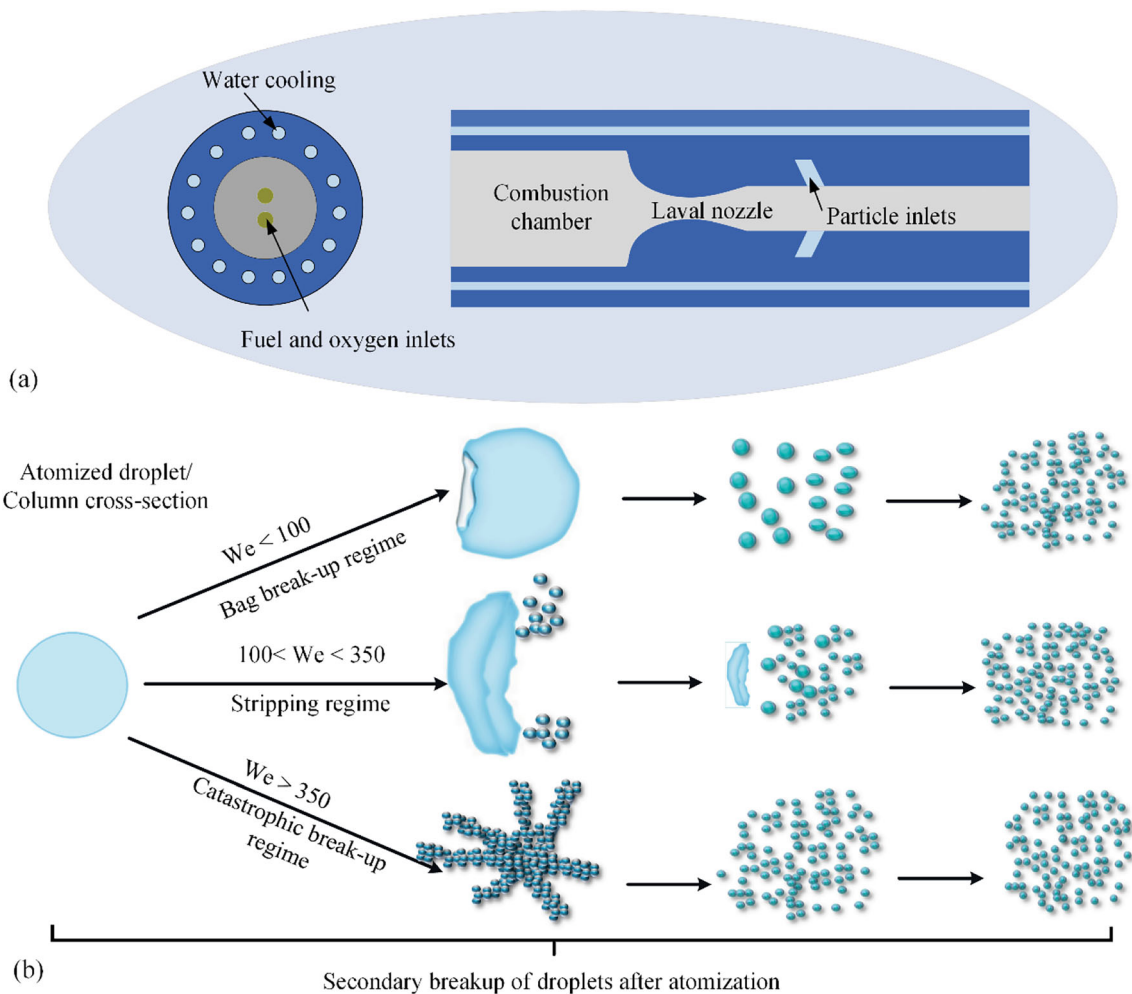


Fig. 1 Schematic diagram of HVOF thermal spraying process and fuel atomization model

implicit algorithm of pressure correlation equation (SIMPLE) was used to deal with the coupling of pressure and velocity. The equations were calculated and solved by second-order upwind discretization method.

- The real-time change curve of monitoring variables was used to judge whether the calculation result was convergent. Finally, the post-processing software was used to process the calculation results, and the calculation results were verified and comprehensively analyzed.

Gas Phase Dynamics Model

In the Euler–Lagrange method, gases were modeled as continuous phases. The conservation equations of the mass, momentum, energy, and species transport for gas phase can be ideally represented by Cartesian tensor coordinate systems [15, 17].

Conservation of mass

$$\frac{\partial(\rho\mu_i)}{\partial x_i} + \frac{\partial\rho}{\partial t} = 0 \tag{Eq 1}$$

Conservation of energy

$$\frac{\partial}{\partial x_i} [u_i(\rho E + P)] + \frac{\partial}{\partial t} (\rho E) = \frac{\partial}{\partial x_j} \left(k_e \frac{\partial T}{\partial x_j} + u_i(\tau_{ij})_e \right) + S_t \tag{Eq 2}$$

Conservation of momentum

$$\frac{\partial}{\partial t} (\rho u_i) + \frac{\partial}{\partial x_j} (\rho u_i u_j) = -\frac{\partial p}{\partial x_i} + \frac{\partial}{\partial x_j} (\tau_{ij})_e + \frac{\partial}{\partial x_j} (-\overline{\rho u_i' u_j'}) \tag{Eq 3}$$

Species transport

$$\frac{\partial}{\partial x_i} (\rho Y_\alpha u_i) = -\frac{\partial J_{\alpha,i}}{\partial x_i} + R_\alpha + S_\alpha \quad \alpha = 1, 2, \dots, N - 1 \tag{Eq 4}$$

Combustion Model

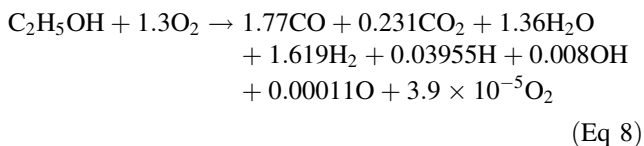
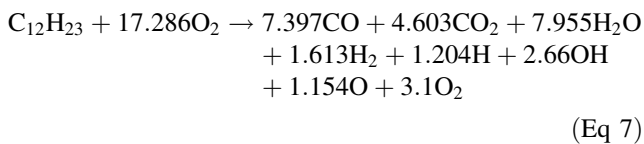
In the JP-8000 HVOF spraying system, fuel droplets are atomized by a coaxial atomizer before entering the combustion chamber. Specifically, the coaxial atomizer is responsible for atomizing the larger liquid fuel droplets into small droplets, and then sending the atomized small fuel droplets into the combustion chamber for combustion. To save calculation time, the relevant calculation of atomizing process of fuel droplets (large droplet to small droplet) by coaxial atomizer is ignored. In this study, the calculation model starts from the combustion chamber area, where small fuel droplets and oxygen enter the combustion chamber after premixing. Because the atomized droplets are small in diameter and quickly evaporate in the combustion chamber with a high temperature and pressure, this study assumes that the overall reaction rate is controlled by turbulent mixing, and unknown chemical reaction kinetic rates are safely ignored (Ref 18). Based on the work of Magnussen and Hjertager (Ref 19, 20), FLU-ENT provides a turbulence chemical reaction interaction model, that is, Eddy dissipation model (EDM), which is commonly used to simulate the combustion in the HVOF process (Ref 21).

The production rate $R_{i,r}$ of substance i in the reaction r is given by the smaller of the following two expressions [16]

$$R_{i,r} = v''_{i,r} M_i A \rho \frac{\varepsilon}{k} \min \left(\frac{Y_R}{v_{R,r} M_i} \right) \tag{Eq 5}$$

$$R_{i,r} = v''_{i,r} M_i A B \rho \frac{\varepsilon}{k} \left(\frac{\sum_P Y_P}{\sum_J v''_{j,r} M_j} \right) \tag{Eq 6}$$

Under ideal conditions, the complete combustion products of the kerosene and ethanol are CO_2 and H_2O . However, the flame flow temperature is up to 3000 K during the spraying, and the combustion products will be dissociated, including not only combustible gases such as CO and H_2 , but also atomic gases such as O , H , OH produced by dissociation. Based on the chemical equilibrium procedure developed by Sanford and Bonnie J (Ref 22), the chemistry of kerosene and alcohol is as follows (Ref 12, 15):



Turbulence Model

The realizable $k-\varepsilon$ turbulence model, as a supplement to the standard $k-\varepsilon$ model and the RNG $k-\varepsilon$ model, considers the Boussinesq relation and the definition of vortex viscosity to obtain the compressible flow equation under normal Reynolds pressure (Ref 23, 24). The realizable $k-\varepsilon$ model based on the Reynolds-averaged Navier–Stokes equations (RANS) has the following form (Ref 9, 25).

Turbulent kinetic energy

$$\begin{aligned} \frac{\partial}{\partial r}(r\rho kv_r) + \frac{\partial}{\partial x}(r\rho kv_x) &= \frac{\partial}{\partial x} \left(r \left(\mu + \frac{\mu_t}{\sigma_k} \right) \frac{\partial k}{\partial x} \right) \\ &+ \frac{\partial}{\partial r} \left(r \left(\mu + \frac{\mu_t}{\sigma_k} \right) \frac{\partial k}{\partial r} \right) \\ &+ r(G_k + G_b - \rho\varepsilon - Y_M) \end{aligned} \tag{Eq 9}$$

Turbulence dissipation rate

$$\begin{aligned} \frac{\partial}{\partial x}(r\rho\varepsilon v_x) + \frac{\partial}{\partial r}(r\rho\varepsilon v_r) &= \frac{\partial}{\partial r} \left(r \left(\mu + \frac{\mu_t}{\sigma_\varepsilon} \right) \frac{\partial \varepsilon}{\partial r} \right) \\ &+ \frac{\partial}{\partial x} \left(r \left(\mu + \frac{\mu_t}{\sigma_\varepsilon} \right) \frac{\partial \varepsilon}{\partial x} \right) \\ &+ r \left(\rho C_1 S\varepsilon - \rho C_2 \frac{\varepsilon^2}{k + \sqrt{v\varepsilon}} + \rho C_{1\varepsilon} \frac{\varepsilon}{k} C_{2\varepsilon} G_b \right) \end{aligned} \tag{Eq 10}$$

Turbulent viscosity

$$\mu_t = \rho C_\mu \frac{k^2}{\varepsilon} \tag{Eq 11}$$

Dynamic viscosity coefficient

$$C_\mu = \frac{1}{A_0 + A_s(kU^*/\varepsilon)} \tag{Eq 12}$$

Discrete Phase Model

In Euler–Lagrange method, the Lagrange trajectory model was used to simulate the motion and heat transfer of particles, which can be divided into the stochastic model and the deterministic model. A stochastic model was used in this study, which considers the effects of gas turbulence on particle motion and heat transfer. In this study, WC-12Co particles and fuel droplets were regarded as discrete phases. The Kelvin–Helmholtz Rayleigh–Taylor (KHRT) method and O’Rourke method in the discrete phase model were used to deal with the breakup and coalescence of fuel droplets. The KHRT model combines the Kelvin–Helmholtz instability theory and Rayleigh–Taylor instability theory, which can more accurately simulate the breakup and atomization process of droplets in high shear airflow, and then more accurately predict the size and distribution of droplets. The O’Rourke method assumes that the

collision can occur only when two droplet groups exist in the same fluid grid, and consider the collision probability and subsequent coalescence of the droplet, and the method has second-order precision in space.

Discrete Phase Droplets

Fuel droplets undergo three physical processes of heating, evaporation and boiling during combustion. When the temperature of fuel droplets is lower than the evaporation temperature, no mass transfer occurs. The heat transfer equation is as follows:

$$m_s c_s \frac{dT_s}{dt} = Sh(T_g - T_s) + \varepsilon_s A_s \sigma (\theta_s^4 - T_s^4) \tag{Eq 13}$$

Heat transfer coefficient

$$h = Nu \frac{\chi_g}{d_s} \tag{Eq 14}$$

The Nusselt number (Nu) is derived from the Lowndes and Marshall correlation

$$Nu = 2.0 + 0.6Pr^{1/3}Re_p^{1/2} \tag{Eq 15}$$

When the temperature of the fuel droplets reaches the evaporation temperature, mass transfer occurs and the mass of fuel droplets begins to decrease, its mass transfer equation is

$$m_s(t + \Delta t) = m_s(t) - Nu_{AB} SM_{\omega,j} \Delta t \tag{Eq 16}$$

The mass transfer coefficient is

$$Nu_{AB} = 2.0 + 0.6Re_p^{1/2} Sc^{1/3} \tag{Eq 17}$$

The heat transfer equation is

$$m_s c_s \frac{dT_s}{dt} = Sh(T_g - T_s) + \varepsilon_s A_s \sigma (\theta_s^4 - T_s^4) + \frac{dm_s}{dt} h_{fg} \tag{Eq 18}$$

When the temperature of the fuel droplet reaches the boiling point, the temperature remains unchanged, and the mass transfer equation is

$$\frac{d(d_s)}{dt} = \frac{4k_e}{\rho_s c_{s,g} d_s} (1 + 0.23\sqrt{Re_p}) \ln \left[1 + \frac{c_{s,g}(T_g - T_s)}{h_{fg}} \right] \tag{Eq 19}$$

The droplet boiling evaporation rate is

$$\frac{d(d_s)}{dt} = \frac{2}{\rho_s h_{fg}} \left[\frac{k_e [1 + 0.23\sqrt{Re_p}]}{d_s} (T_g - T_s) + \varepsilon_s \sigma (\theta_s^4 - T_s^4) \right] \tag{Eq 20}$$

Discrete Phase Particle

To analyze the heat transfer and melting behavior of WC-12Co particles during HVOF thermal spraying, it is necessary to consider the complex interaction of multiphase flow, heat transfer and particle phase transition.

Particle Dynamics In spraying, the force acting on the particles is mainly the drag force, and the influence of the gravity, thermophoresis force and Brownian force are ignored (Ref 26, 27)

$$\frac{du_p}{dt} = F_p(u' - u_p) + \frac{g(\rho_p - \rho)}{\rho_p} + F_x \tag{Eq 21}$$

$F_p(u' - u_p)$ is the drag force in unit mass of the particles, in which

$$F_p = \frac{18\mu_x C_D Re_p}{\rho_p d_p^2 24} \tag{Eq 22}$$

Re_p is the relative Reynolds number, defined as

$$Re_p = \frac{\rho d_p |u_p - u|}{\mu} \tag{Eq 23}$$

Particles and droplets are defined as spheres, and drag coefficients [28] are as follows:

$$C_D = a_1 + \frac{a_2}{Re_p} + \frac{a_3}{Re_p} \tag{Eq 24}$$

In which

$$a_1, a_2, a_3 = \left\{ \begin{array}{ll} 0, 24, 0 & 0 < Re_p < 0.1 \\ 3.690, 22.73, 0.0903 & 0.1 < Re_p < 1 \\ 1.222, 29.1667, -3.8889 & 1 < Re_p < 10 \\ 0.6167, 46.50, -116.67 & 10 < Re_p < 100 \\ 0.3644, 98.33, -2778 & 100 < Re_p < 1000 \\ 0.357, 148.62, -47500 & 1000 < Re_p < 5000 \\ 0.46, -490.546, 578700 & 5000 < Re_p < 10000 \\ 0.5191, -1662.5, 5416700 & Re_p \geq 10000 \end{array} \right. \tag{Eq 25}$$

Particle Heat Transfer In the process of thermal spraying, the Biot number of particles is usually less than 0.1. Assuming that the temperature gradient inside the particles is zero (Ref 29). Newton’s cooling law and radiation heat transfer equation were used to solve convection and radiation heat transfer between particles and ambient fluids. The heat transfer equation between the single particle and the continuous phase can be simplified to a first-order ordinary differential equation (Ref 12), as shown in Eq. (13).

Particle Phase Transformation The phase transition model of the particles was enabled, and the melting point, latent heat, and phase transition temperature of the particles was set in the material properties. Considering the latent heat effect of particles during phase transition, the energy balance equation of phase transition is as follows:

$$\frac{\partial}{\partial t}(\rho H) + \nabla \cdot (\rho \vec{v} H) = \nabla \cdot (k_0 \nabla T) + S \tag{Eq 26}$$

The enthalpy value H is

$$H = h + \beta h_{fg} \tag{Eq 27}$$

The fluid (molten state) fraction β is

$$\beta = \begin{cases} 0 & \text{if } T_p < T_{\text{solidus}} \\ 1 & \text{if } T_p > T_{\text{liquidus}} \\ \frac{T_p - T_{\text{solidus}}}{T_{\text{liquidus}} - T_{\text{solidus}}} & \text{if } T_{\text{solidus}} < T_p < T_{\text{liquidus}} \end{cases} \tag{Eq 28}$$

Particle Size The particles of WC-12Co were prepared by agglomeration sintering method with uneven size distribution. The microscopic morphology and size distribution of the particles are shown in Fig. 2.

Figure 2(b) shows that there are more particles with size of 15-35 μm in the sprayed powder. Therefore, to save calculation costs under actual spraying conditions, 15-35 μm was selected as the particle size in the simulation calculation, and three particle sizes (the minimum value of 15 μm , the maximum of 35 μm , and the average diameter of 23.09307) were determined. The Rosin-Rammler method (Ref 7) was used to describe the particle size distribution. The functional relationship between particle size and mass fraction is

$$Y_d = e^{-(d/\bar{d})^n} \tag{Eq 29}$$

Geometric Structure and Meshing

The computational domain geometry model of JP-8000 spray gun is shown in Fig. 3. To save calculation time and cost, we set up the axisymmetric two-dimensional model of JP-8000 gun to calculate while ensuring the accuracy of calculation results. The calculation area is divided into two parts, one is the gun geometry model as the internal flow field, and the other is the rectangular region as the external flow field with a width of 300 mm and a height of 220 mm.

The essence for computational fluid dynamics is to make point discretization or region dispersion of the regions specified by the control equation. Therefore, the grid quality significantly influences the calculation accuracy, efficiency and stability of the solver. ICEM software was used for the structured meshing of the computation area. Figure 4 shows a grid calculation model in two-dimensional consisting of the combustion chamber, nozzle, barrel and air domain. The grid of combustion chamber, Laval nozzle and parallel barrel were finely divided to improve the calculation accuracy. The entire computation area contains 87,055 nodes and 85,196 cells.

The nozzle and combustion chamber were set as non-slip walls at an initial temperature of 300 K. The inlet boundary was set as the mass flow inlet, and the turbulence intensity was 5%. The outlet boundary was set as the pressure outlet, and the initial pressure was 1 atm. The spraying distance was 300 mm, and the substrate temperature was 500 K. The WC-12Co particles were radially fed into the gun in surface form through Inlet 2 at an initial rate of 10 m/s. The premixed ethanol-kerosene fuel droplets

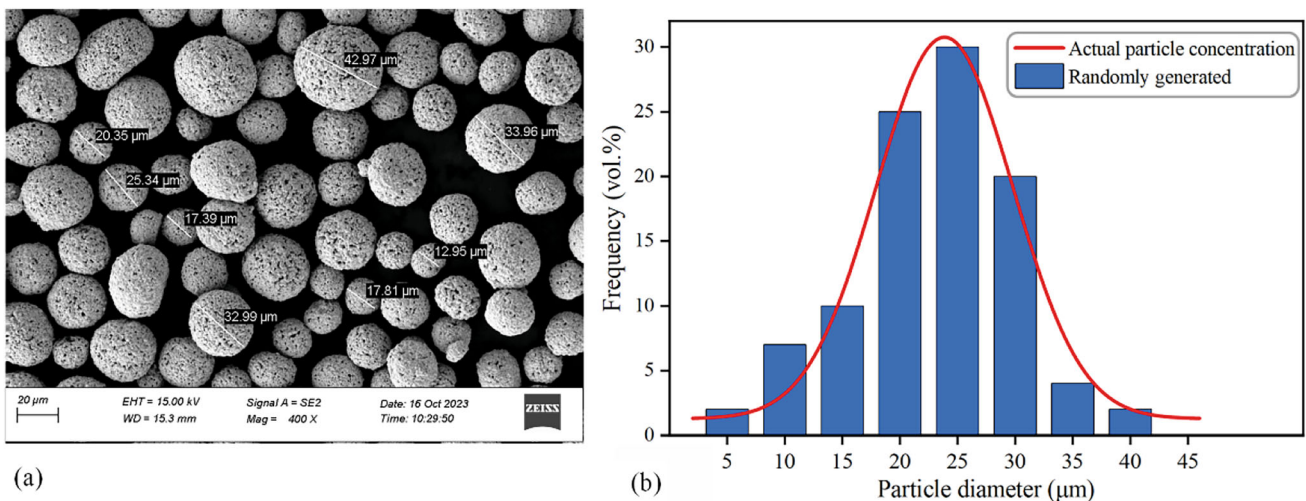


Fig. 2 Microscopic morphology and size distribution of the particles

Fig. 3 Computational domain geometry model of JP-8000 gun

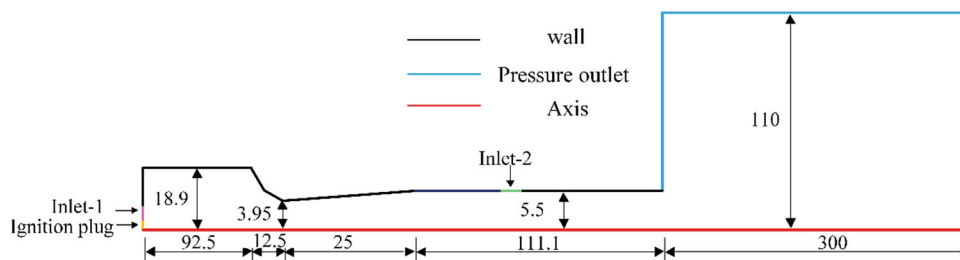


Fig. 4 Meshing of the calculated areas (a) global grid, (b) combustion chamber, (c) Laval nozzle, and (d) free jet area

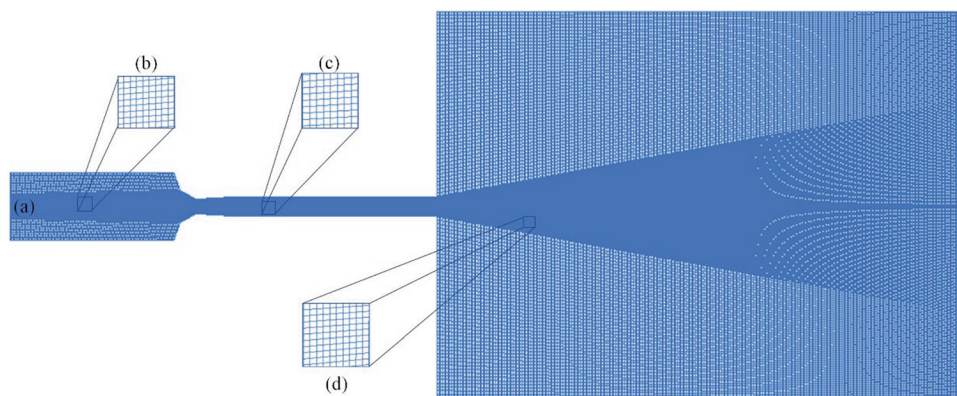


Table 1 Physicochemical property of C₁₂H₂₃ and C₂H₅OH

Fuel	Calorific value, J/kg	Specific heat capacity, J/kg K	Viscosity, Pa s	Density, kg/m ³
C ₁₂ H ₂₃	4.30×10^7	5.75×10^5	2.5×10^{-3}	0.8×10^3
C ₂ H ₅ OH	2.97×10^7	6.58×10^5	1.2×10^{-3}	0.789×10^3

after atomization were injected into the gun in surface form through Inlet 1 at an initial rate of 10 m/s. Considering that the atomization process may be affected by other process parameters, the size of the fuel droplets after atomization was set to a random distribution based on the Rosin-Rammler method. The droplet size (the minimum value of 0.001 mm, the maximum of 0.006 mm, and the average diameter of 0.0035 mm) in this paper was determined according to that weighted average diameters of the primary child droplets was about 0.0035mm in Ref (9) , and the droplet size diffusion coefficient was calculated for 1.1717645. Table 1 shows the physical properties of the two fuels. The oxygen/fuel ratio was 3.5, and the mass flow of fuel and oxygen was 0.00847 kg/s and 0.03 kg/s, respectively. The effects of ethanol proportion on flow field and particle flight behavior in HVOF spraying were analyzed with the proportion of ethanol in total fuel as a single variable. Table 2 shows the process parameters of six groups for numerical simulation.

Analysis of Computing Result

Model Validation

At present, there have been some researches on mixed combustion of spray fuel, but the researches on the influence of ethanol-kerosene ratio on gas–solid two-phase flow characteristics are limited. There is a relative lack of detailed research on mixed combustion for ethanol-kerosene in thermal spraying process. Therefore, the kerosene fuel (C₁₂H₂₃) was used to verify the model effectiveness under same process parameters in this study. The contour plot of flame flow variation for base case during spraying is shown in Fig. 5. The maximum velocity of the flame flow is 2119 m/s, the maximum temperature is 3385 K, and the maximum pressure is 859939 Pa. All parameters meet the requirements of spraying conditions, and obvious Mach cones can be observed at the spray gun outlet and in the air domain, which is consistent with the actual spraying situation.

Figure 6 shows the changes of the flame flow along the central axis during the spraying in base case. The flame flow velocity reaches the maximum at the gun outlet. Due

Table 2 Description of researched cases

Case	Aviation kerosene mass flow, kg/s	Alcohol mass flow, kg/s	Alcohol ratio, %
Base case	0.00847	0	0
Case 1	0.007623	0.000847	10
Case 2	0.005929	0.002541	30
Case 3	0.004235	0.004235	50
Case 4	0.7392	0.001848	70
Case 5	0	0.00847	100

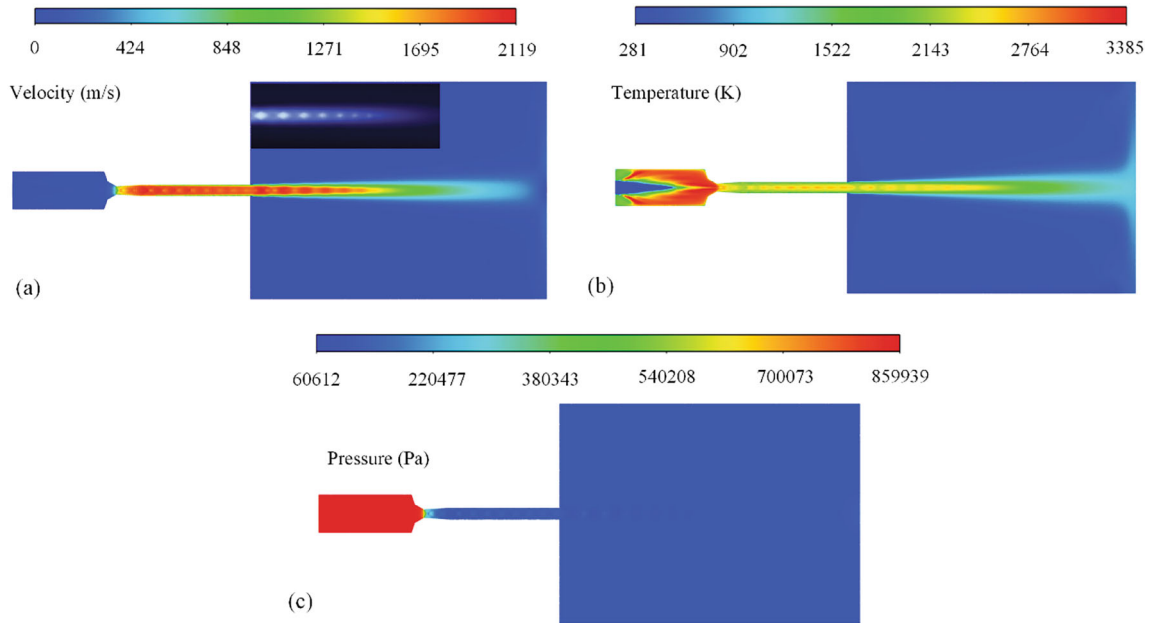


Fig. 5 Contour plot of flame flow variation in base case during spraying (a) velocity, (b) temperature, (c) pressure

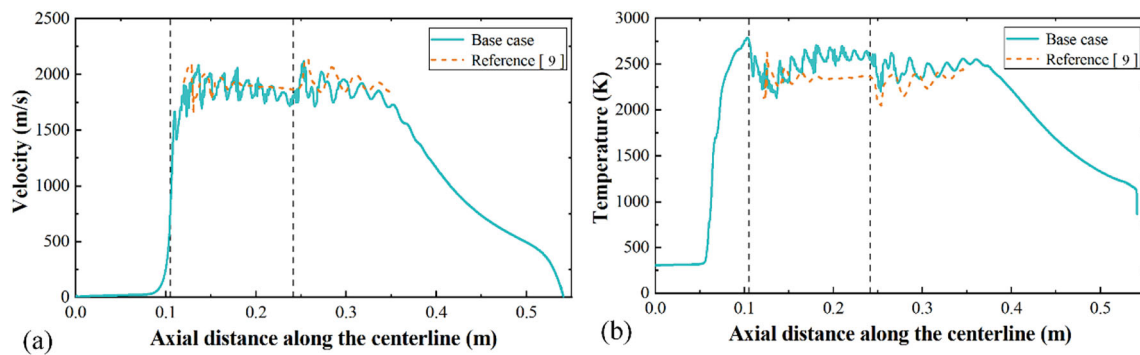


Fig. 6 Changes of flame flow in base case along the central axis during spraying (a) velocity, (b) temperature

to the convergent and divergent action of Laval nozzle, the heat energy converges, and the flame flow temperature reaches the maximum at the nozzle. The calculated results are highly consistent with those of H. Tabbara et al. (Ref 9), which verifies the validity of the model presented in this study. The gas velocity during HVOF spraying is usually very high, even exceeding the sound speed, and the compressibility effect can enhance the capture for turbulent

characteristics under high Mach number flow, and more accurately calculate the interaction force and heat transfer between particles and the gas flow. Therefore, the compressibility effect is considered in this model, so that the prediction of turbulence intensity and the fluctuation degree of the flame flow is enhanced, the flame flow characteristics in the local region sharply change, and the nozzle and the barrel show more violent fluctuations. Also

due to compressibility effect, seven distinct Mach cones can be observed at the gun outlet in this model, while there are only five Mach cones in the literature (Ref 9). Relevant experiments also show that the spraying flame flow can reach up to 7-9 Mach numbers in the actual spraying process (as shown in Fig. 5a), which further proves the accuracy of this model.

Analysis of Flame Flow Results

Figure 7 shows the contour plot of flame flow velocity change under different ethanol proportion. In Case 1, the flame flow velocity is the highest, which is 2360 m/s, an increase of 11.4% compared with base case. This is because ethanol is less viscous and more volatile, and it is easy to quickly evaporate in the atomization process, which promotes the combustion of kerosene, and the fuel burns more fully, releasing more energy. In Case 2 and Case 3, the maximum flame flow velocity is 2193 m/s and 2118 m/s, respectively, which is close to the flame flow velocity (2119 m/s) in base case. In Case 4 and Case 5, the flame flow velocity decreases by 8% and 11.8%, respectively, and the maximum velocity is only 1947 m/s and 1869 m/s, and no clear Mach occurs at the gun outlet. The results indicate that the energy released by combustion decreases

with the increase in ethanol proportion when the ethanol proportion is higher than 10%, and the flame flow does not provide sufficient kinetic energy for the spraying particles when the ethanol proportion is higher than 70%.

Figure 8 shows the change contour plot of flame flow temperature under different ethanol proportion. The temperature characteristics for flame flow of kerosene combustion and ethanol-kerosene combustion in the combustion chamber are obviously different. The addition of the ethanol reduces the viscosity of the fuel, and makes the fuel flow more easily. The flight path of different fuel droplets after entering the combustion chamber is different under the influence for the flame flow. In the base case, kerosene fuel droplets gather near the centerline of the combustion chamber, and combustion starts from both sides of the droplets stream. Due to that the calorific value of the kerosene is relatively high, the red high-temperature area fills the combustion chamber, and the maximum temperature for the flame flow is 3385 K. Due to the full combustion of the mixed fuel, the maximum temperature for flame flow in Case 1 is 3503 K, which increases by 3.5% compared with the base case. The maximum temperatures of flame flow in Case 2, Case 3, Case 4 and Case 5 are 3260 K, 2923 K, 2562 K and 2275 K, which decrease by 3.7%, 13.6%, 24.3% and 33.8% compared with

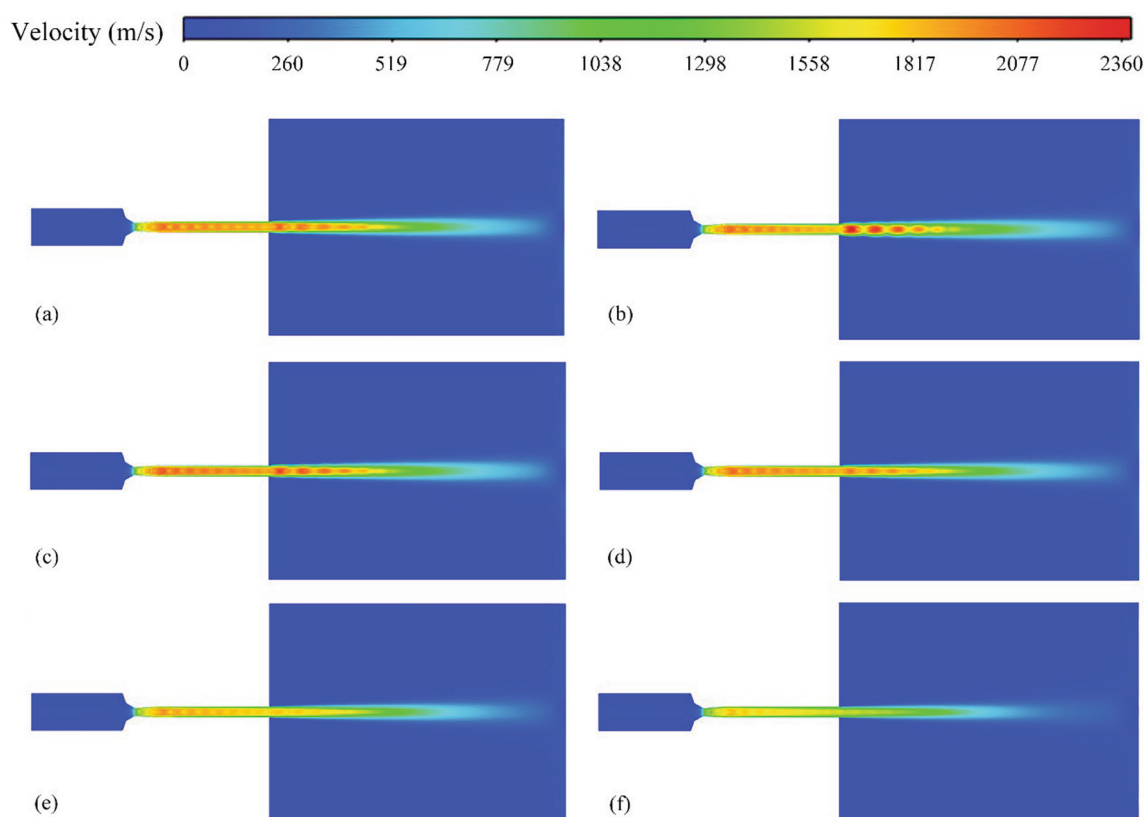


Fig. 7 Change contour plots of flame flow velocity under different ethanol proportions (a) Base case, (b) Case 1, (c) Case 2, (d) Case 3, (e) Case 4, (f) Case 5

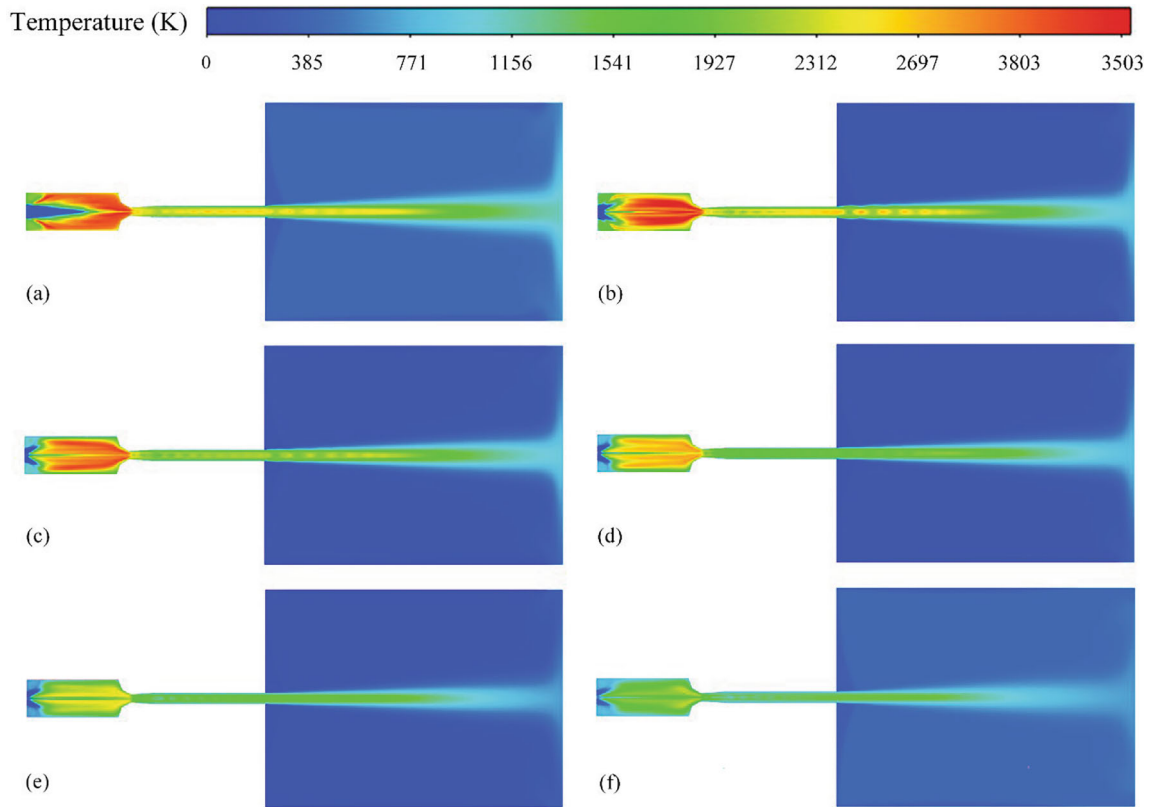


Fig. 8 Change contour plots of flame flow temperature under different ethanol proportions (a) Base case, (b) Case 1, (c) Case 2, (d) Case 3, (e) Case 4, (f) Case 5

base case, respectively. The results indicate that when the ethanol proportion is higher than 10%, the energy released by combustion decreases with the increase in the ethanol proportion, and when the ethanol proportion is higher than 70%, the flame flow cannot provide enough heat energy for the spraying particles.

Figure 9 shows the change contour plot of flame flow pressure under different ethanol proportions. The pressure in Case 1 is the highest, which is 948801 Pa, an increase of 10.3% compared with base case. This is due to that the addition for a small amount of ethanol promotes the combustion of kerosene fuel, and more gas is generated from the reaction and gathers in the combustion chamber. The maximum pressure of flame flow in Case 2 is 887588 Pa, which increases by 3.2% compared with base case. In Case 3, Case 4 and Case 5, the maximum pressure of flame flow is 821699, 745302 and 625837 Pa, which decrease by 4.4, 13.3 and 27.2% compared with base case, respectively. The results indicate that when the ethanol proportion is higher than 30%, the flame flow pressure decreases with the increase in the ethanol proportion. In Case 4 and Case 5, the pressure is poor, and no obvious fluctuation can be observed at the spray gun outlet. The flame flow in the air domain has a weak acceleration effect on particles, which affects the coating quality.

Figure 10 is the changes of flame flow along the central axis under different ethanol proportions. Figure 10(a) shows that there is no significant difference in the flame flow velocity of the combustion chamber. Through the acceleration of the Laval nozzle, the velocity of the flame flow rapidly rises, and that of Case 3 in the parallel nozzle is the highest. With the increase in the spraying distance, the flame flow velocity slowly decreases in a “fluctuation.” In the air domain, due to the full combustion of the flame flow, the gas pressure is high, and the pressure difference for flame flow at the nozzle outlet of Case 1 is large. That causes the external air flow to fluctuate violently, presenting a diamond-like waveform with compression wave and expansion wave, and the highest velocity peak. As the ethanol proportion increases, the fluctuation becomes smoother. For Fig. 10(b), pure kerosene fuel in the base case has a long ignition lag period due to high viscosity and low volatility. The addition of ethanol in aviation kerosene fuel accelerates the breaking of droplets, forming finer atomized droplets, and the combustion reaction is advanced, almost immediately burning when fuels enter the combustion chamber. Compared with the ethanol fuel, kerosene fuel has a higher calorific value, so the increase in ethanol proportion reduces the overall heat release from the combustion. In Fig. 10(c), due to sufficient

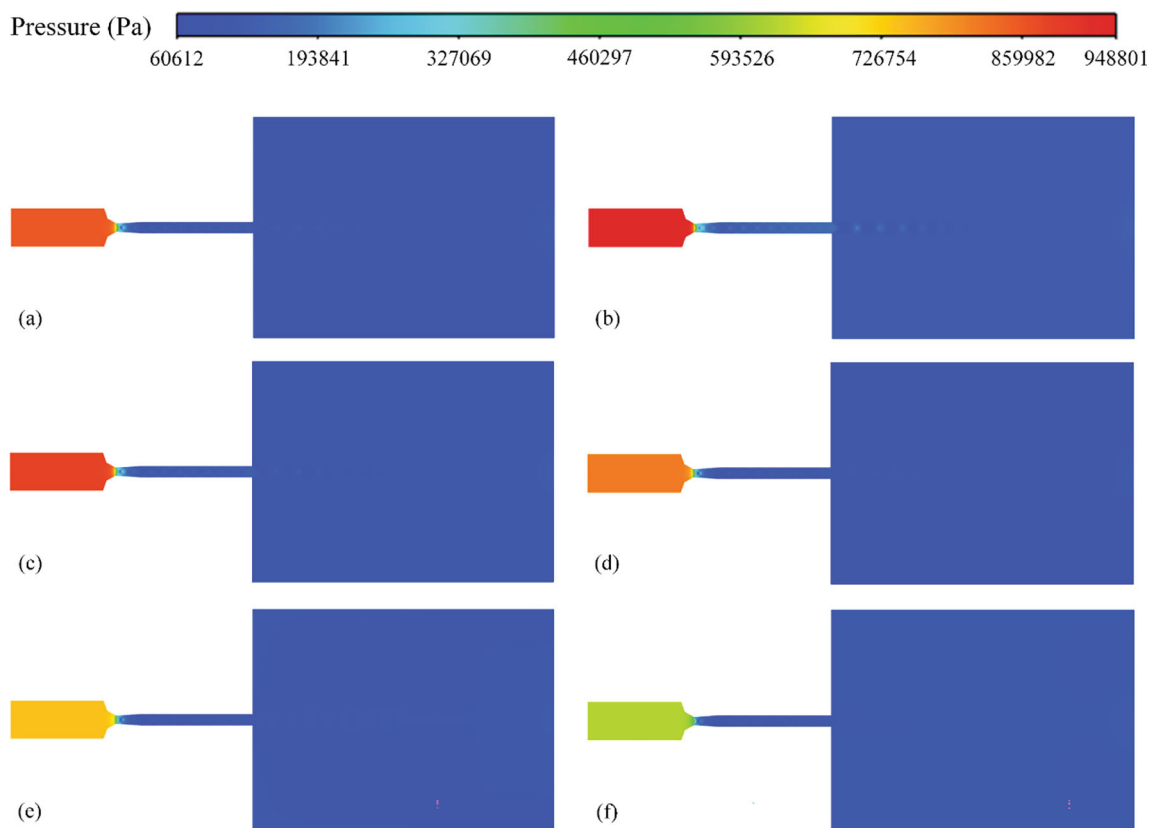


Fig. 9 Change contour plots of flame flow pressure under different ethanol proportions (a) Base case, (b) Case 1, (c) Case 2, (d) Case 3, (e) Case 4, (f) Case 5

combustion, a large number of product gases generated by the combustion are concentrated, the flame flow pressure in Case 1 is always highest. In summary, the flame flow generated by the combustion of ethanol-kerosene mixed fuel for Case 1 has the characteristics of high kinetic energy and high thermal energy, the energy utilization rate is the highest, which meets the requirements of spraying conditions.

Figure 11 shows the vector diagram of flame velocity change in the combustion chamber during the spraying in base case and Case 1. In base case, kerosene fuel is more viscous, the attraction between molecules is greater, and after entering the combustion chamber, it is less affected by the flame flow, the ability to maintain axial velocity is stronger. The droplets gather at the centerline of the gun body, and the breakup, atomization and combustion preferentially occur at the front end and both sides of the agglomerated droplet. In Case 1, the addition for ethanol reduces the viscosity of the fuel mixture, and the movement of fuel droplets is more susceptible to the influence of flame flow. As can be seen from the local magnification of the flame flow velocity, the flame flow has a radial velocity when mixed fuel is used, which makes the fuel droplets spread to both sides. The mixed fuel droplets faster occur

breakup, atomization and combustion in the combustion chamber, and the axial displacement is smaller. There is reverse velocity between the two fuel inlets, and complex turbulent behavior exists in the local region, which further leads to the failure of the two fuel droplets to converge.

Figure 12 shows the changes of CO_2 and CO mass fraction along the central axis under different ethanol proportions. There is a small difference between the mass fraction of CO_2 and CO at the spray gun outlet in base case and Case 1. With the increasing ethanol proportion, the mass fraction of CO_2 obviously decreases, and the mass fraction of CO slightly increases. This is because both kerosene and ethanol combustion products contain CO and CO_2 gases, but for the same molar mass, kerosene fuels produce more carbon emissions (as shown by the reaction equation). Therefore, as the ethanol ratio in Cases 1-5 successively increases, the CO_2 content decreases. At the same time, because ethanol gas is relatively unstable, CO gas will be pyrolysis at high temperature, resulting in a slight increase in CO content with the increasing ethanol ratio. As can be seen from Fig. 12(b), near the spraying distance $x = 0.34$ m, the CO emission gap between different ethanol proportions is smaller than that at the spray gun outlet. This is due to the further reaction between the

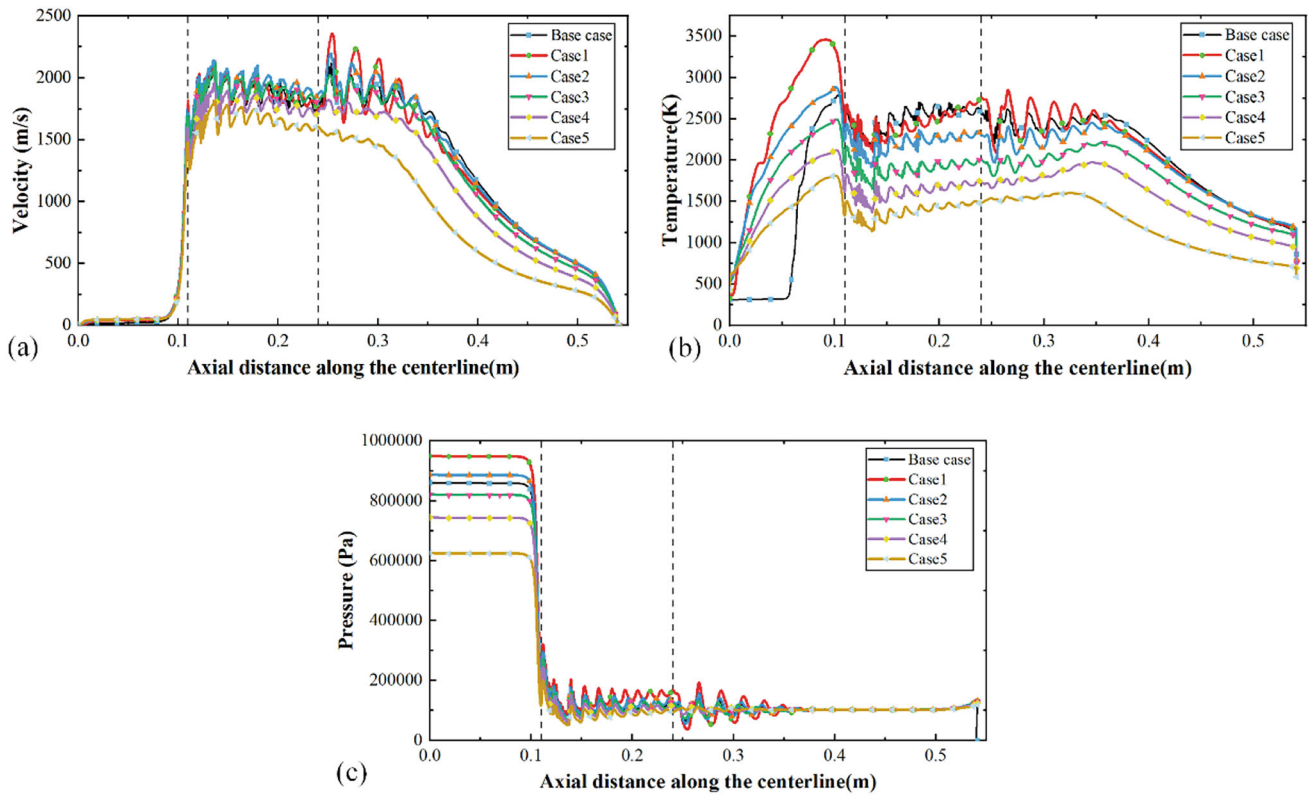
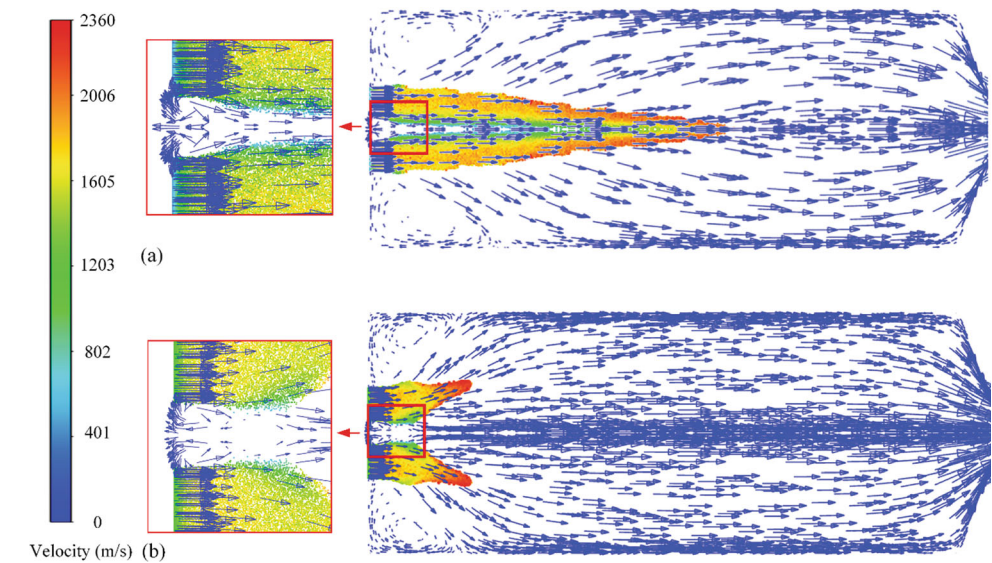


Fig. 10 Changes of flame flow along the central axis under different ethanol proportions (a) velocity, (b) temperature, (c) pressure

Fig. 11 Vector diagram of flame velocity change in the combustion chamber during the spraying (a) Base case, (b) Case 1



CO produced by pyrolysis inside the spray gun and the oxygen in the air domain to produce CO₂. The same mass flow of kerosene fuel and ethanol-kerosene mixed fuel, because of the higher carbon proportion in kerosene, combustion produces more CO₂. The changes of CO₂ and CO mass fractions at the gun outlet are shown in Table 3. The reduction rate of CO₂ emissions increases with the increasing ethanol proportion, and the growth rate of CO

emissions decreases with the increasing ethanol proportion. To sum up, the ethanol-kerosene mixed fuel can effectively reduce CO₂ emissions on the basis of ensuring the original spraying conditions, and the impact for CO produced by ethanol pyrolysis can be mitigated by oxygen-enriched combustion.

Figure 13 shows the changes of fuel mass fraction and combustion reaction rate under different ethanol

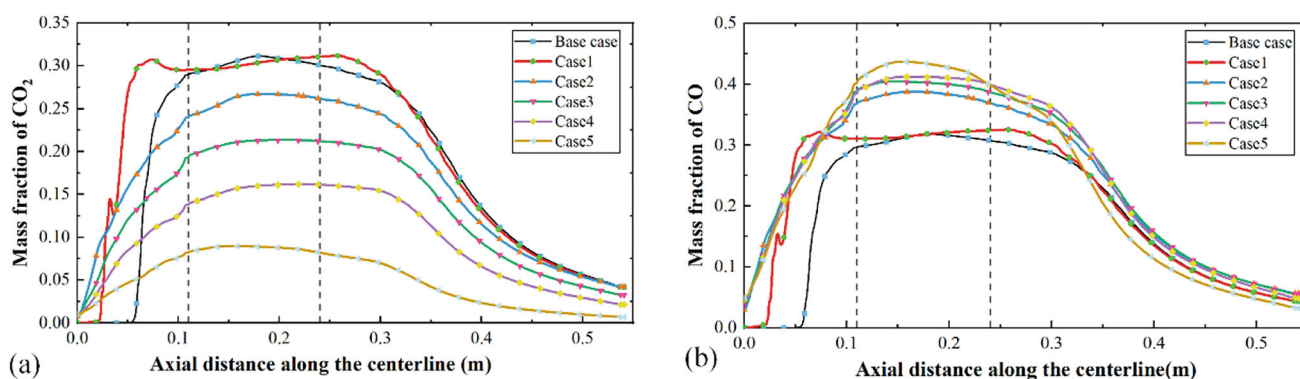


Fig. 12 Mass fraction changes of CO₂ and CO along the central axis under different ethanol proportions (a) CO₂, (b) CO

Table 3 Mass fraction of CO₂ and CO at the spray gun outlet

Case	CO ₂ mass fraction, wt.%	CO mass fraction, wt.%	Alcohol ratio
Base case	0.30	0.31	0%
Case 1	0.31(↑3.3%)	0.32(↑3.2%)	10%
Case 2	0.26(↓13.3%)	0.36(↑16.1%)	30%
Case 3	0.21(↓30.0%)	0.38(↑22.6%)	50%
Case 4	0.16(↓46.7%)	0.39(↑25.8%)	70%
Case 5	0.08(↓73.3%)	0.39(↑25.8%)	100%

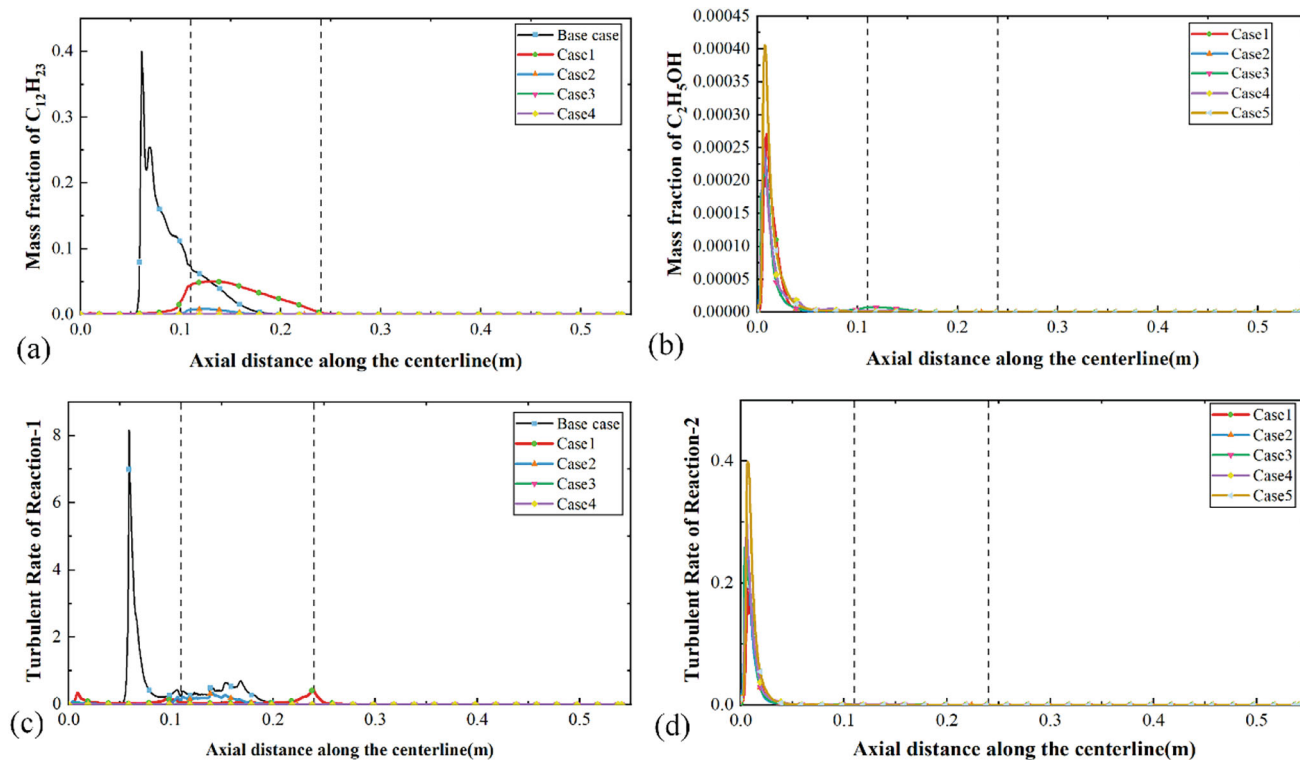
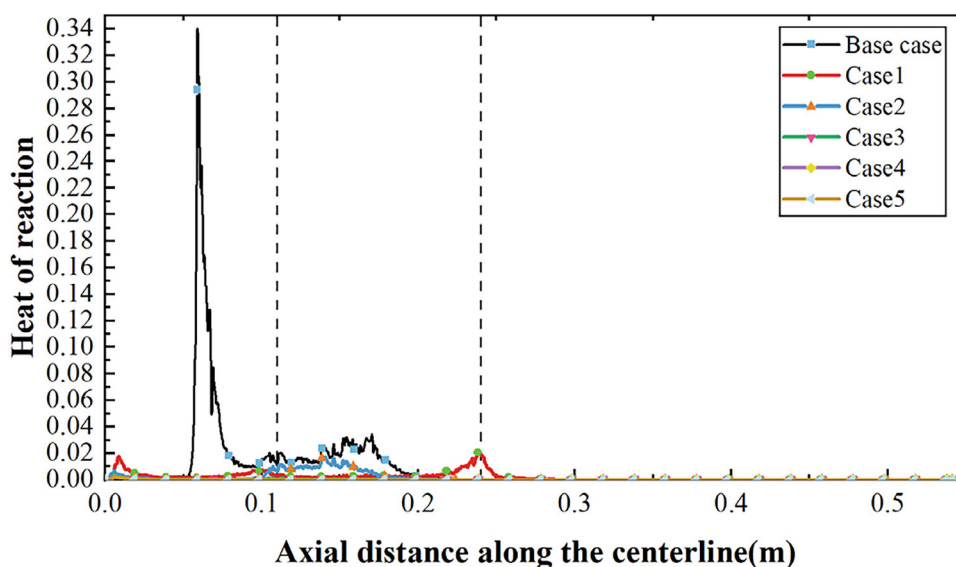


Fig. 13 Mass fraction variation of fuel and turbulent reaction rate under different ethanol proportions (a) C₁₂H₂₃ mass fraction, (b) C₂H₅OH mass fraction, (c) reaction 1 rate, (d) reaction 2 rate

proportions in spraying process. The mass fraction change of $C_{12}H_{23}$ is shown as Fig. 13(a). In base case, the kerosene fuel exists as liquid in the first half of the combustion chamber. Near the axial distance $x = 0.05$ m, kerosene droplets begin to evaporate, and the mass fraction of $C_{12}H_{23}$ in the combustion chamber rapidly increases. Combined with Fig. 13(c), the combustion reaction immediately begins after the kerosene evaporates into gas, and the turbulence rate of reaction 1 rapidly increases. With the increasing ethanol proportion, the viscosity of the mixed fuel decreases, the intermolecular forces reduce, part of the kerosene begins to evaporate after entering the combustion chamber, and then is immediately consumed by the combustion reaction. Therefore, Case 1 presents a fluctuation peak for reaction 1 turbulent rate at the front of the combustion chamber. The oxygen is exhausted in the second half of the combustion chamber, the $C_{12}H_{23}$ mass fraction begins to accumulate, encountering air from the outside in the parallel barrel, and the turbulence rate of reaction 1 fluctuates again. From Fig. 13(b) and (d), the evaporate and combustion of ethanol fuel occurs before those of kerosene fuel, which further verifies that the addition for ethanol fuel causes the combustion reaction to occur earlier and the fuel ratio in Case 1 promotes the combustion.

Figure 14 shows the change of combustion reaction heat along the central axis under different ethanol proportions in spraying. The change trend of the overall combustion reaction heat is similar to the reaction turbulence rate for kerosene fuel. With the increasing ethanol proportion, the heat release of overall reaction decreases, indicating that the heat energy in spraying is mainly derived from kerosene fuel.

Fig. 14 Change of combustion reaction heat along the central axis under different ethanol proportions in spraying



The Result Analysis of Particles and Fuel Droplets

Figure 15 shows the change of $C_{12}H_{23}$ fuel droplets under different ethanol proportions during the spraying. As the ethanol proportion increases, the viscosity of the mixed fuel droplets decreases, and they are more prone to breakup and evaporation. After breakup, the fine fuel droplets are easily affected by the flame flow, and the distribution range gradually spreads from the centerline of the combustion chamber to the wall direction. As the ethanol proportion increases, the more obvious the diffusion behavior, the velocity of broken droplets gradually increases. The maximum droplet velocity of base case is only 23.23 m/s, and that of Case 5 can reach 33.07 m/s. The maximum droplet temperature of base case is only 496 K, and that of Case 1 slightly increases to 501.5 K. In other cases, the droplet temperature decreases with the increasing ethanol proportion, but the range of red high-temperature region gradually expands. From Fig. 15(iii), both droplet breakup and evaporation occur at the edge of the agglomerated droplet. As ethanol proportion increases, the region for breakup becomes larger due to the decrease in viscosity.

Figure 16 shows the change of C_2H_5OH fuel droplets under different ethanol proportions during the spraying. The fuel droplets change of C_2H_5OH is basically the same as that of $C_{12}H_{23}$. The droplet velocity maximum of Case 1 is only 23.86 m/s, that of Case 5 increased to 43.11 m/s. In Case 1, the droplet temperature is low, and the maximum value is only 352.5 K. In Case 2, the maximum value is highest for 359.9 K. In other cases, the droplet temperature decreases with the increasing ethanol proportion, but the high-temperature range gradually expands. Compared with $C_{12}H_{23}$ fuel droplets, the high-temperature region of C_2H_5OH fuel droplets is smaller, which is due to the large

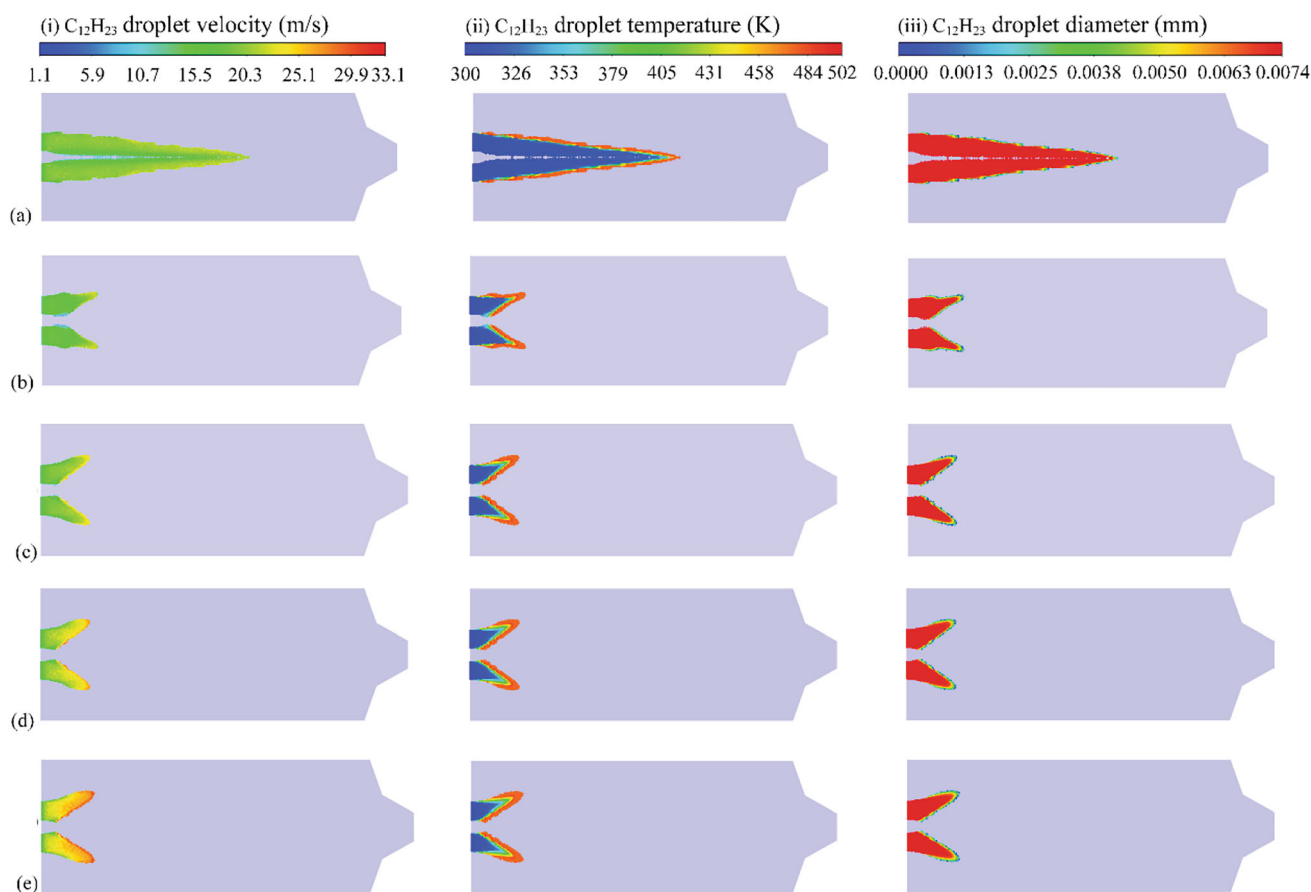


Fig. 15 Change of $C_{12}H_{23}$ fuel droplets under different ethanol proportions (a) Base case, (b) Case 1, (c) Case 2, (d) Case 3, (e) Case 4

specific heat capacity for C_2H_5OH with strong heat absorption ability and slow temperature growth. The droplet velocity of C_2H_5OH fuel is larger, which is due to its small viscosity, strong fluidity, and more obvious droplets breakage.

Figure 17 shows the temperature change of spraying particles for three particle sizes under different ethanol proportions during the spraying. The flight time of particles with three sizes is obviously different. The particles with the smallest size are obviously heated and accelerated by flame flow, the flight time is the shortest, and the particle temperature first reaches the maximum. And due to its small mass and inertia, the ability to maintain the flight state is poor, it is easily affected by external cold air, and the particle characteristics significantly decline after reaching the maximum. Table 4 shows the highest particle temperature of three sizes under different ethanol proportions during the spraying. The addition for a little ethanol promotes the heating of spraying particles, and when the ethanol proportion exceeds 30%, the heating of spraying particles is restrained. In this study, WC-12Co was used as spraying particle material, with the solid phase temperature of 1580 K, the liquid phase temperature of 1640 K, and the

bonded phase Co with a melting point of 1768 K. To ensure that the spraying particles hit the substrate in a molten or semi-molten state, the suitable temperature of spraying particles should be kept in the range of 1580–1768 K. In summary, when the particle size is small ($d = 15 \mu\text{m}$), to avoid the ablation of the spraying particles caused by high temperature, the fuel with high ethanol proportion should be selected (Case 3, Case 4). When the particle size is relatively large ($d = 23 \mu\text{m}$), the fuel with poor ethanol proportion should be selected (Case 1, Case 2). When the particle size is greater than $35 \mu\text{m}$, the particle temperature is poorer than the solid phase temperature, and the particles will hit the substrate in a solid state, causing the low coating bonding strength.

Figure 18 shows the velocity change of the spraying particles with three sizes under different ethanol proportions during the spraying. The change trend of particle velocity is basically consistent with particle temperature. The maximum velocity of particles with three sizes under different ethanol proportions in the spraying process are shown in Table 5. Particles with larger size ($d = 35 \mu\text{m}$) are less accelerated by flame flow, resulting in low kinetic energy of sprayed particles, and the particle velocity range

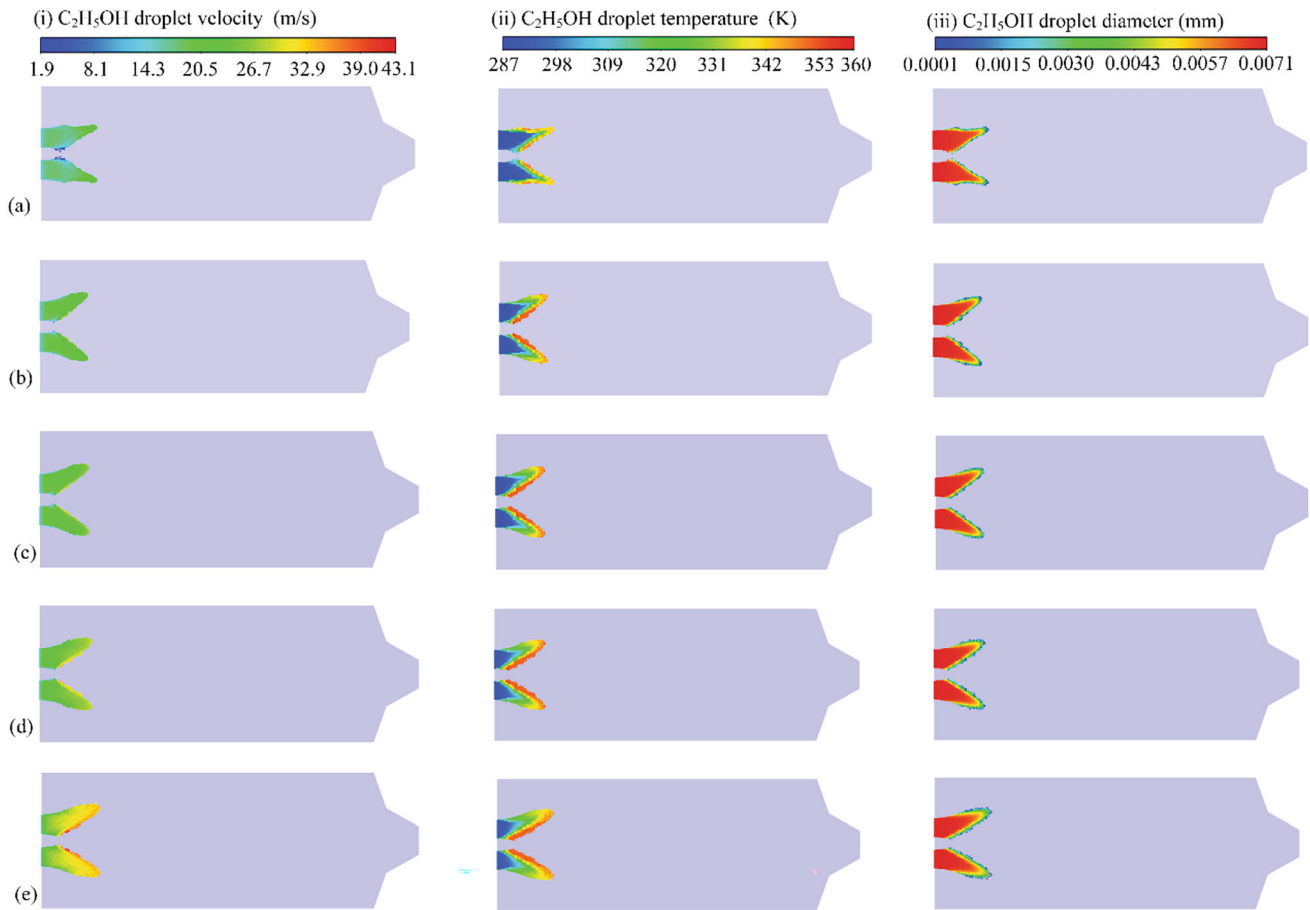


Fig. 16 Change of C_2H_5OH fuel droplets under different ethanol proportions (a) Case 1, (b) Case 2, (c) Case 3, (d) Case 4, (e) Case 5

is only 308–380 m/s under different ethanol proportions. That causes weak impact force when the particles impact substrate, and low coating bonding strength. The flame flow in Case 2 actively effects the acceleration of spraying particles. In other cases, the higher the ethanol proportion, the stronger the inhibition effect on the acceleration of spraying particles. This is due to that the acceleration of the flame to the particles mainly occurs inside the parallel nozzle, where the flame velocity of Case 2 is the highest, and the acceleration effect on particles is the strongest. The high velocity of particles facilitates rapid flattening after particles impacting the substrate to form a high-quality coating.

Conclusion

To practice the concept of green environmental protection and promote the green development for industry, this study simulates the HVOF spraying process using ethanol-kerosene mixed fuel on the basis of the existing spraying process parameters. The ethanol-kerosene mixed fuel was injected into the JP-8000 spray gun in discrete phase, and

the Kelvin–Helmholtz Rayleigh–Taylor (KHRT) breakup model was used to describe the breakup of aviation kerosene and ethanol droplets. The random distribution of WC-12Co particle sizes was realized by the Rosin-Rammler method. The effects of ethanol proportion in fuel on flame flow characteristic, fuel droplet breaking and gasification process and particle flight behavior during spraying were explored.

1. The calculation result of flame flow shows that adding a certain amount of ethanol to the kerosene fuel can provide enough kinetic and thermal energy for the spraying process. In this study, the ratio of mixed fuel under Case 1 promotes the combustion reaction and effectively improves the energy utilization rate.
2. As the ethanol proportion increases, the mass fraction of CO_2 at the gun outlet obviously decreases, and the mass fraction of CO slightly increases. This indicates that ethanol-kerosene mixed fuel can effectively reduce CO_2 emissions on the basis of ensuring the original spraying conditions, and the CO_2 emissions can be reduced by 30% (Case 3). For the slight increase in CO emissions caused by ethanol pyrolysis,

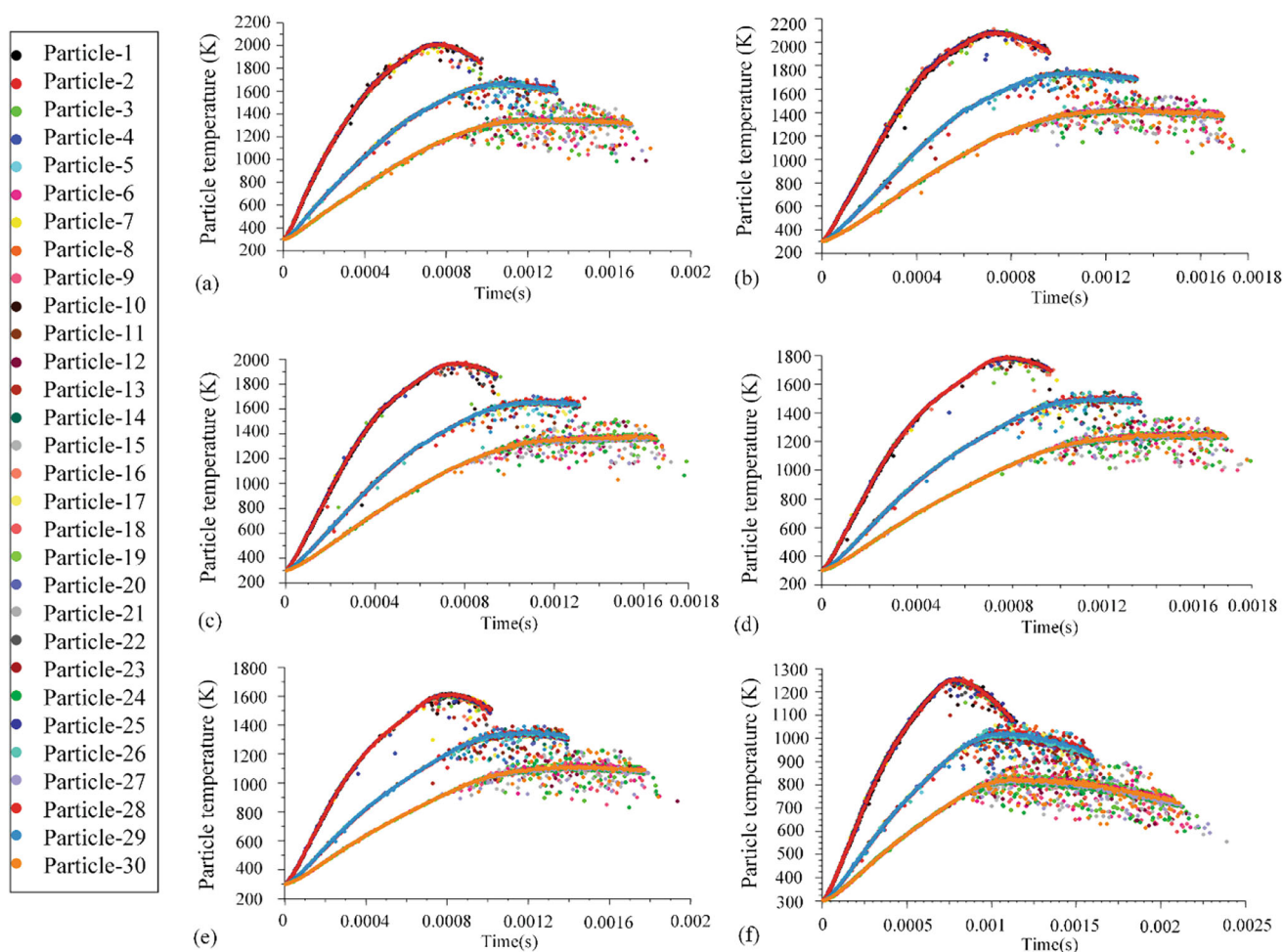


Fig. 17 Temperature change of spraying particles for three particle sizes under different ethanol proportions (a) Base case, (b) Case 1, (c) Case 2, (d) Case 3, (e) Case 4, (f) Case 5

Table 4 Maximum temperature of particles with three sizes

Case	Maximum temperature ($d = 15 \mu\text{m}$)	Maximum temperature ($d = 23 \mu\text{m}$)	Maximum temperature ($d = 35 \mu\text{m}$)
Base case	2009 K	1678 K	1483 K
Case 1	2073 K ($\uparrow 3.2\%$)	1756 K ($\uparrow 4.6\%$)	1516 K ($\uparrow 2.2\%$)
Case 2	1969 K ($\downarrow 2.0\%$)	1690 K ($\uparrow 0.7\%$)	1512 K ($\uparrow 2.0\%$)
Case 3	1788 K ($\downarrow 11.0\%$)	1512 K ($\downarrow 9.9\%$)	1350 K ($\downarrow 9.0\%$)
Case 4	1618 K ($\downarrow 19.5\%$)	1386 K ($\downarrow 17.4\%$)	1224 K ($\downarrow 17.5\%$)
Case 5	1253 K ($\downarrow 37.6\%$)	1061 K ($\downarrow 36.8\%$)	918 K ($\downarrow 38.1\%$)

oxygen-enriched combustion can be used to alleviate the impact.

- When the particle size is small ($d = 15 \mu\text{m}$), to avoid the ablation of spraying particles caused by high temperature, the fuel with high ethanol proportion should be selected (Case 3, Case 4). When the particle

size is relatively large ($d = 23 \mu\text{m}$), the fuel with low ethanol proportion should be selected (Case 1, Case 2). When the particle size is higher than $35 \mu\text{m}$, the maximum particle temperature is too small, which will reduce the coating bonding strength. The smaller the

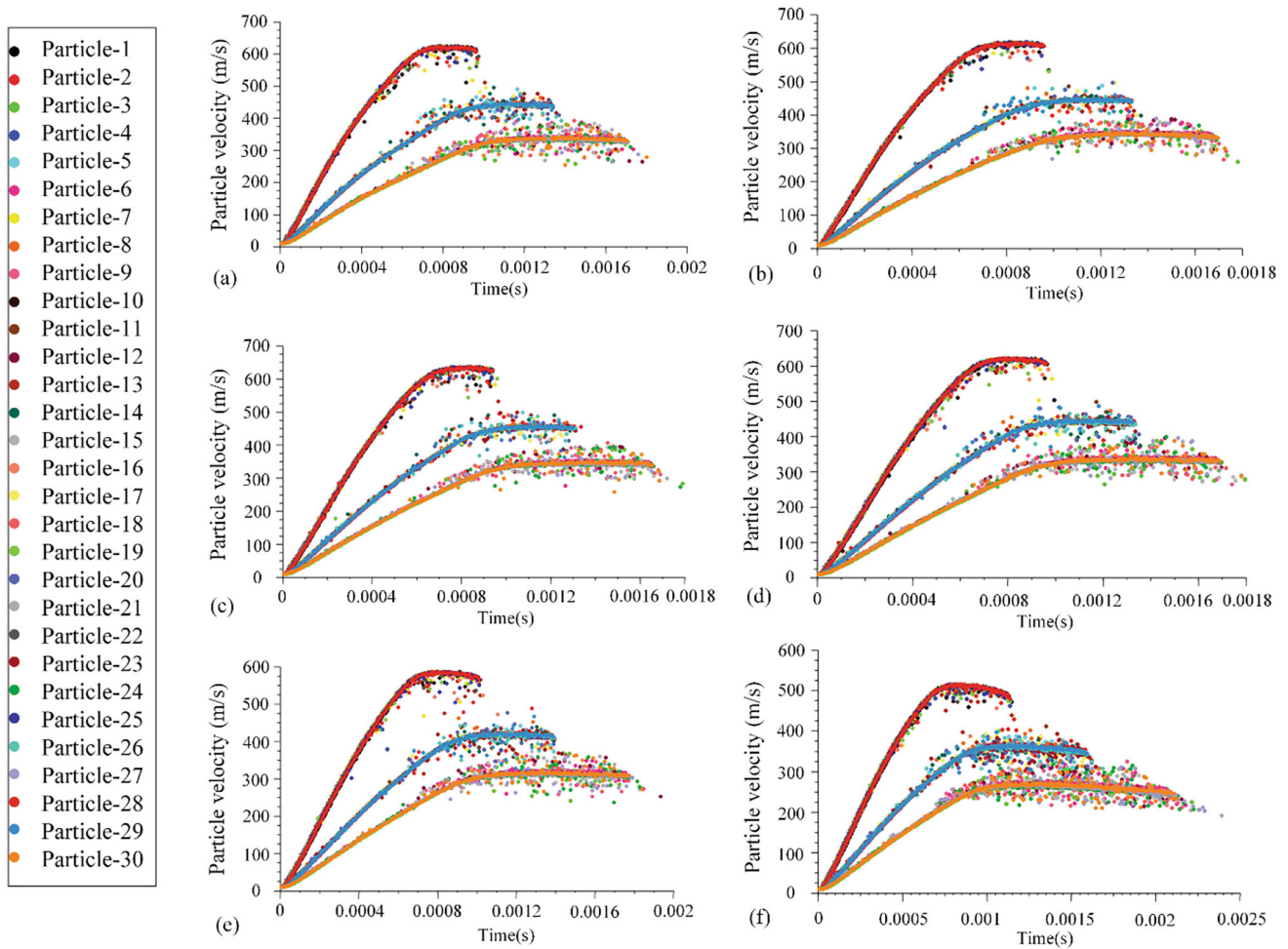


Fig. 18 Velocity change of spraying particles for three particle sizes under different ethanol proportions (a) Base case, (b) Case 1, (c) Case 2, (d) Case 3, (e) Case 4, (f) Case 5

Table 5 Maximum velocity of particles with three sizes

Case	Maximum velocity ($d = 15 \mu\text{m}$)	Maximum velocity ($d = 23 \mu\text{m}$)	Maximum velocity ($d = 35 \mu\text{m}$)
Base case	624 m/s	463 m/s	383 m/s
Case 1	616 m/s (↓1.3%)	460 m/s (↓0.6%)	380 m/s (↓0.8%)
Case 2	636 m/s (↑2.0%)	496 m/s (↑7.1%)	388 m/s (↑1.3%)
Case 3	622 m/s (↓0.3%)	456 m/s (↓1.5%)	389 m/s (↑1.6%)
Case 4	586 m/s (↓6.0%)	487 m/s (↑5.2%)	369 m/s (↓3.7%)
Case 5	515 m/s (↓17.5%)	404 m/s (↓12.7%)	308 m/s (↓19.6%)

particle size, the larger the velocity of the particle when it hits the substrate.

Acknowledgments This work was supported by Applied Basic Research Program of Liaoning Province (2023JH2/101300226), Project for Graduate Education Reform and Technological Innovation and Entrepreneurship of University of Science and Technology Liaoning (2023YJSCX02).

Author Contributions Siyu Li involved in software, data curation, formal analysis, and writing—original draft. Chang Li involved in funding acquisition and project administration. Pengfei Liu involved in methodology and visualization. Xing Han involved in writing—review and editing.

Data Availability No data were used for the research described in the article.

Declarations

Conflict of interest The authors declare that they have no known competing financial interests or personal relationships that could have appeared to influence the work reported in this study.

References

1. L. Jacobs, M.M. Hyland, and M. De Bonte, Comparative Study of WC-Cermet Coatings Sprayed Via the HVOF and the HVAF Process, *ASM Int.*, 1998, **7**, p 213-218.
2. G. Wang, Z. Huang, P. Xiao, and X. Zhu, Spraying of Fe-Based Amorphous Coating with High Corrosion Resistance by HVAF, *J. Manuf. Process.*, 2016, **22**, p 34-38.
3. S.L. Liu, X.P. Zheng, and G.Q. Geng, Influence of Nano-WC-12Co Powder Addition in WC-10Co-4Cr AC-HVAF Sprayed Coatings on Wear and Erosion Behaviour, *Wear*, 2010, **269**, p 362-367.
4. D. Cheng, G. Trapaga, J.W. McKelliget, and E.J. Lavernia, Mathematical Modelling of High Velocity Oxygen Fuel Thermal Spraying of Nanocrystalline, *Modell. Simul. Mater. Sci. Eng.*, 2002, **11**, p 1-13.
5. L. Zhao, M. Maurer, F. Fischer, and E. Lugscheider, Study of HVOF Spraying of WC-CoCr Using On-Line Particle Monitoring, *Surf. Coat. Technol.*, 2004, **185**, p 160-165.
6. C.F. You and X.C. Xu, Coal Combustion and its Pollution Control in China, *Energy*, 2010, **35**, p 4467-4472.
7. N.C. Wu, K. Chen, W.H. Sun, and J.Q. Wang, Correlation Between Particle Size and Porosity of Fe-Based Amorphous Coating, *Surf. Eng.*, 2018, **35**, p 37-45.
8. J. Patra, P. Ghose, A. Datta, M. Das, R. Ganguly, S. Sen, and S. Chatterjee, Studies of Combustion Characteristics of Kerosene Ethanol Blends in an Axi-Symmetric Combustor, *Fuel*, 2015, **144**, p 205-213.
9. H. Tabbara and S. Gu, A Study of Liquid Droplet Disintegration for the Development of Nanostructured Coatings, *AIChE J.*, 2012, **58**, p 3533-3544.
10. X. Wang, Q. Song, and Z. Yu, Numerical Investigation of Combustion and Flow Dynamics in a High Velocity Oxygen-Fuel Thermal Spray Gun, *J. Therm. Spray Technol.*, 2015, **25**, p 441-450.
11. S. Liu, H. Wu, S. Xie, M.-P. Planche, D. Rivolet, M. Moliere, and H. Liao, Novel Liquid Fuel HVOF Torches Fueled with Ethanol: Relationships Between In-Flight Particle Characteristics and Properties of WC-10Co-4Cr Coatings, *Surf. Coat. Technol.*, 2021, **408**, p 126805.
12. M. Jadidi, S. Moghtadernejad, and A. Dolatabadi, Numerical Modeling of Suspension HVOF Spray, *J. Therm. Spray Technol.*, 2015, **25**, p 451-464.
13. S. Kamnis and S. Gu, Study of In-Flight and Impact Dynamics of Nonspherical Particles from HVOF Guns, *J. Therm. Spray Technol.*, 2009, **19**, p 31-41.
14. S. Gu and S. Kamnis, Numerical Modelling of In-Flight Particle Dynamics of Non-Spherical Powder, *Surf. Coat. Technol.*, 2009, **203**, p 3485-3490.
15. J. Pan, S. Hu, L. Yang, K. Ding, and B. Ma, Numerical Analysis of Flame and Particle Behavior in an HVOF Thermal Spray Process, *Mater. Des.*, 2016, **96**, p 370-376.
16. S. Kamnis and S. Gu, 3D Modelling of Kerosene-Fuelled HVOF Thermal Spray Gun, *Chem. Eng. Sci.*, 2006, **61**, p 5427-5439.
17. S. Kamnis and S. Gu, Numerical Modelling of Propane Combustion in a High Velocity Oxygen-Fuel Thermal Spray Gun, *Chem. Eng. Process.*, 2006, **45**, p 246-253.
18. M.N. Khan and T. Shamim, Investigation of a Dual-Stage High Velocity Oxygen Fuel Thermal Spray System, *Appl. Energy*, 2014, **130**, p 853-862.
19. B.F. Magnussen, B. Hjertager, On mathematical modeling of turbulent combustion with special emphasis on soot formation and combustion, 16: 719-729. (1977)
20. B.F. Magnussen, B.H. Hjertager, J.G. Olsen, and D. Bhaduri, Effects of turbulent structure and local concentrations on soot formation and combustion in C₂H₂ diffusion flames, 17: 1383-1393. (1979)
21. R. Kamali and A.R. Binesh, The Importance of Sensitive Parameters Effect on the Combustion in a High Velocity Oxygen-Fuel Spray System, *Int. Commun. Heat Mass Transf.*, 2009, **36**, p 978-983.
22. S. Gordon, B.J. McBride, Computer program for calculation of complex chemical equilibrium compositions and applications. Part 1: Analysis. Nasa reference publications. (1994)
23. J. Yu, X. Liu, Y. Yu, Z. Li, S. Xu, H. Li, P. Liu, and L. Wang, Effect of HVOF Spraying Process on Particle Behavior of Fe-Based Amorphous Alloy Coatings, *J. Therm. Spray Technol.*, 2022, **31**, p 2448-2462.
24. S.G.S. Kamnis, Numerical Modelling of Propane Combustion in a High Velocity Oxygen-Fuel Thermal Spray Gun, *Chem. Eng. Process.*, 2006, **45**, p 246-253.
25. X. Zhao, C. Li, S. Li, H. Jiang, and X. Han, Time-Varying Evolutionary Mechanism Analysis of the Multiphase Flow During High-Velocity Oxygen-Fuel (HVOF) Thermal Spraying WC-12Co Particle, *Surf. Coat. Technol.*, 2023, **461**, p 129435-129450.
26. M.N. Khan and T. Shamim, Effect of Particle and Injection Parameters on the Performance of a Dual-Stage High-Velocity Oxygen Fuel Thermal Spray System, *J. Therm. Spray Technol.*, 2015, **24**, p 1-10.
27. M.N. Khan and T. Shamim, Effect of Operating Parameters on a Dual-Stage High Velocity Oxygen Fuel Thermal Spray System, *J. Therm. Spray Technol.*, 2014, **23**, p 910-918.
28. S. Morsi and A. Alexander, An Investigation of Particle Trajectories in Two-Phase Flow Systems, *J. Fluid Mech.*, 1972, **55**(2), p 193-208.
29. D. Cheng, Q. Xu, G. Trapaga, and E.J. Lavernia, The Effect of Particle Size and Morphology on the In-Flight Behavior of Particles During High-Velocity Oxyfuel Thermal Spraying, *Metall. Mater. Trans. B*, 2001, **32**, p 525-535.

Publisher's Note Springer Nature remains neutral with regard to jurisdictional claims in published maps and institutional affiliations.

Springer Nature or its licensor (e.g. a society or other partner) holds exclusive rights to this article under a publishing agreement with the author(s) or other rightsholder(s); author self-archiving of the accepted manuscript version of this article is solely governed by the terms of such publishing agreement and applicable law.